Nano Energy 156 (2026) 112122

Contents lists available at ScienceDirect

Nano Energy

journal homepage: www.elsevier.com/locate/nanoen

Full paper

Hollow-structured piezoelectric acoustic electronics for omnidirectional 3D sound capture

Boling Lan [a], Weili Deng [a,*], Yong Ao [a], Yue Sun [a], Guo Tian [a], Tao Yang [a], Shenglong Wang [a], Longchao Huang [a], Tingting Zhou [a], Peiwen Li [a], Zihan Wang [a], Tianpei Xu [a], Guicen Liu [a], Jinlong Sun [a], Hongguang Li [a], Long Jin [a], Binbin Zhang [c], Fengjun Chun [d], Weiqing Yang [a,b,**]

[a] Key Laboratory of Advanced Technologies of Materials (Ministry of Education), School of Materials Science and Engineering, Southwest Jiaotong University, Chengdu 610031, China
[b] Research Institute of Frontier Science, Southwest Jiaotong University, Chengdu 610031, China
[c] Key Laboratory of Photonic-Electronic Integration and Communication-Sensing Convergence, School of Information Science and Technology, Southwest Jiaotong University, Chengdu 611756, China
[d] Institute of Biomedical Engineering, College of Medicine, Southwest Jiaotong University, Chengdu 610031, China

ARTICLE INFO

Keywords:
Hollow-structured
Omnidirectional capture
Piezoelectric polymer
High-performance
Acoustic electronics

ABSTRACT

Piezoelectric polymer-based acoustic electronics hold great potential for human-machine interaction in intelligent acoustic systems, owing to their inherent wideband characteristics. However, conventional acoustic electronics are often constrained by unidirectional response, poor signal-to-noise ratio (SNR), and low sensitivity. To address these challenges, we propose a controllable, hollow-structured piezoelectric nanofiber that simultaneously optimizes the intrinsic crystallization behavior and acoustic absorption of PVDF. This approach enables the fabrication of a high-performance hollow nanofiber-based acoustic sensor (HAS). The resulting HAS demonstrates a maximum sensitivity of 418 mV/Pa, a 209% improvement over leading reference sensors, together with a 365% enhancement in SNR (290 ± 4.7 dB) and a 500% increase in frequency resolution (0.1 Hz) compared to state-of-the-art and commercial counterparts. By integrating the HAS into a 3D sphere, we demonstrate omnidirectional, high-performance 3D sound recognition and localization, achieving an angular resolution of 10°. This hollow collaborative regulation technology exhibits a promising pathway for advancing piezoelectric bioelectronics.

1. Introduction

Bionic electronics and humanized intelligent robots have garnered significant attention for their unique intelligence and efficiency, positioning them at the forefront of fields such as electronic skin, brain-like computation, and bionic hearing [1–11]. Among them, acoustic sensing has attracted particular interest because it enables non-contact, highly convenient communication through acoustoelectric conversion [12–16]. Continuous advances in materials science have significantly advanced the development of acoustic sensing technologies [17,18]. Significant improvements in the performance of acoustic sensors utilizing triboelectric, capacitive, piezoresistive, and piezoelectric mechanisms have been achieved through various optimization strategies [19–23]. For instance, incorporating different conductive fillers such as carbon nanotubes and MXenes into polymers has enhanced the intrinsic properties of composites, thereby facilitating more efficient acoustic signal monitoring [24–26]. Additionally, the design of diverse micro-nano structures in functional layers, such as pyramid, columnar, and microporous structures, has demonstrated significant potential for achieving high-performance acoustic sensing [27–29]. At the device level, the integration of specialized structures, including aperture designs, kirigami patterns, and piezoelectric ceramic assemblies, has further enhanced acoustic sensing capabilities [30–34]. Despite these advancements, most studies have focused primarily on basic sound recognition, often neglecting the three-dimensional (3D) spatial localization of acoustic signals, which is essential for achieving human-like intelligence in robots. Conventional sound source localization methods, such as microphone arrays or optical techniques, offer high

* Corresponding author.
** Corresponding author at: Research Institute of Frontier Science, Southwest Jiaotong University, Chengdu 610031, China.
E-mail addresses: weili1812@swjtu.edu.cn (W. Deng), wqyang@swjtu.edu.cn (W. Yang).

https://doi.org/10.1016/j.nanoen.2026.112122
Received 7 May 2026; Received in revised form 5 June 2026; Accepted 10 June 2026
Available online 16 June 2026
2211-2855/© 2026 Elsevier Ltd. All rights are reserved, including those for text and data mining, AI training, and similar technologies.

resolution but are hindered by limitations including high cost, significant energy consumption, rigidity, and the need for bulky equipment [35]. Such inherent constraints significantly restrict their applicability in modern intelligent acoustic sensing systems.

Fortunately, flexible piezoelectric nanofibers exhibit exceptional adaptability to low-intensity acoustic vibrations due to their inherent wideband characteristics stemming from high aspect ratio and surface area [36,37]. In contrast to conventional densified membranes, flexible piezoelectric nanofibers demonstrate superior performance, which is achieved through advanced fabrication techniques such as thermal drawing and third-phase doping. These optimized nanofibers have demonstrated broad applicability in acoustic monitoring and recognition, including bidirectional communication and cardiac sound auscultation [20,38–41]. While these developments have laid a solid foundation for acoustic electronics, existing designs have primarily focused on material-level optimization of piezoelectric coefficients, often overlooking the critical acoustic-strain coupling between material characteristics and energy absorption, and the macro-geometric

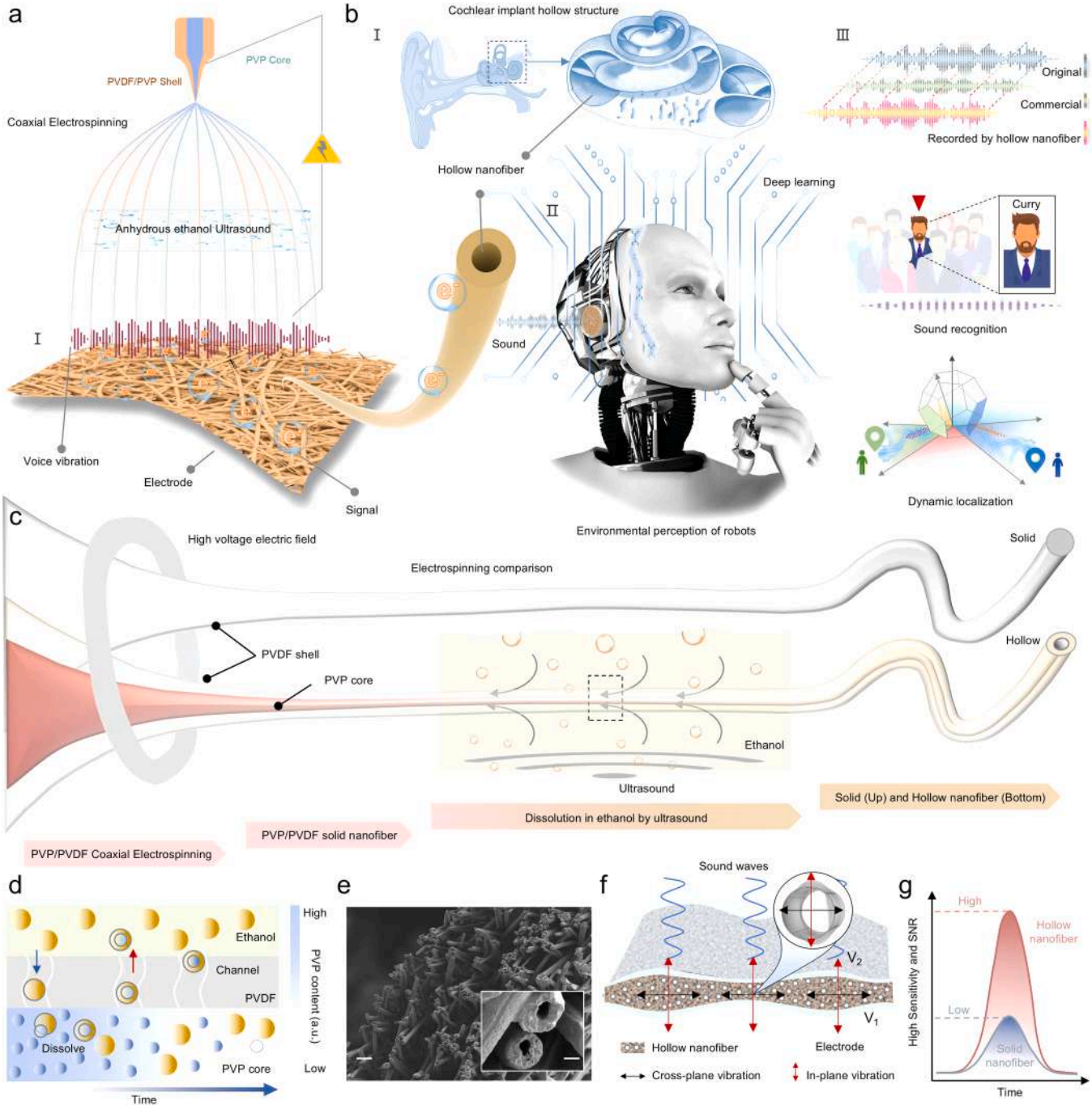


Fig. 1. Overall concept of the hollow nanofiber for smart sound monitoring. a Schematic illustration of hollow nanofiber prepared by coaxial electrospinning; **b** Biomimetic inspiration of the hollow nanofiber membrane and the complex environment, including acoustic monitoring, identification, and spatial dynamic sound localization; **c** Comparison of the preparation processes for solid nanofibers and hollow nanofibers using coaxial electrospinning; **d** Schematic diagram of hollow nanofiber formation by dissolving PVP in ethanol; **e** Cross-sectional SEM image of the hollow nanofibers. Scale bar is 5 μm. The inset shows an enlarged view of the hollow nanofibers. Scale bar is 0.3 μm; **f** Proposed acoustic vibration modes and piezoelectric conversion mechanism for the hollow nanofiber device; **g** Comparison of sensitivity and SNR between hollow nanofibers and solid nanofibers.

configuration of the device for omnidirectional sound capture. This limitation leads to two fundamental bottlenecks: (1) the persistent trade-off between high sensitivity and high SNR, as both depend synergistically on material properties and acoustic energy absorption efficiency; and (2) the inability of planar or simple-curved geometries to achieve uniform omnidirectional sound capture, restricting their use in complex acoustic scenes such as multi-speaker environments.

In this work, we develop a controllable hollow-structured synergistic regulation technology to optimize PVDF's intrinsic crystallization behavior while maximizing acoustic energy absorption. This dual-optimization technology enables unprecedented performance, demonstrating significantly higher sensitivity, SNR, and frequency resolution than existing sensors and commercial membranes. After integrating the hollow-structured PVDF nanofiber into an omnidirectional three-dimensional (3D) sphere (S-HAS), the resulting S-HAS overcomes the limitations of conventional unidirectional sound acquisition and demonstrates omnidirectional capture of spatial sound with an angular resolution of 10°. Assisted by a one-dimensional convolutional neural network (1D-CNN), the S-HAS achieves a sound classification accuracy of 98.83%, significantly outperforming the commercial membrane (93.89%). Due to its excellent acoustoelectric conversion performance, the obtained S-HAS holds great promise for cutting-edge applications such as humanized intelligent robots, bionic electronics, and soft bioelectronics.

2. Results and discussion

2.1. Overall concept of the controllable hollow-structured synergistic regulation technology

Fig. 1**a** schematically depicts the preparation of hollow nanofibers inspired by the hollow structure of cochlear implants via a coaxial electrospinning process. Initially, a mixture solution of polyvinylidene difluoride (PVDF) and polyvinyl pyrrolidone (PVP) was utilized to prepare the outer shell layer, while a pure PVP solution served as the core layer. These solutions were simultaneously electrospun into nanofiber membranes via a coaxial electrospinning method (Supplementary Fig. 1). Subsequently, hollow nanofiber membranes were obtained by dissolving the PVP in ethanol under ultrasonication. Notably, this unique hollow structure endows the nanofibers with excellent acoustoelectric conversion performance, enabling a highly sensitive response to acoustic waves, which in turn meets the stringent requirements of intelligent equipment for weak sound monitoring, identification, and localization in complex environments (Fig. 1**b**). Meanwhile, compared to the conventional electrospinning technique, this coaxial electrospinning technology enables effective control over the specific surface area and crystallization behavior of PVDF by adjusting the thickness of the core layer, thus facilitating the optimization of the acoustoelectric conversion (Fig. 1**c-d**, and Supplementary Note 1). As can be seen from Fig. 1**e**, Supplementary Figs. 2–3, the hollow nanofibers exhibit a uniform and straight morphology on the microscopic scale, with homogeneous pore sizes at their ends. On the macroscopic scale, the hollow nanofibers demonstrate good flexibility, allowing them to be curled arbitrarily. Building on these structural advantages, these hollow nanofibers exhibit enhanced sensitivity and SNR during the acoustoelectric conversion compared to conventional solid nanofibers [44], as illustrated in Fig. 1**f-g**. This performance improvement can be attributed to the unique hollow structure, which simultaneously optimizes the intrinsic crystalline behavior of PVDF for improved electrical output and facilitates greater transverse (V1) and longitudinal (V2) deformations under acoustic excitation, thereby boosting nanofiber electromechanical conversion [39].

2.2. Material characterization and mechanism analysis of the hollow nanofiber

Given that the inner size of hollow nanofibers directly affects the device performance, we conducted an in-depth investigation into the underlying mechanisms. First, hollow nanofibers with different inner sizes were prepared by modulating PVP concentration (0%, 10%, 20%, and 30%), labeled as R0, R1, R2, and R3, respectively (Fig. 2**a**). To analyze the variation in hollow diameter quantitatively, we performed mathematical statistics on the outer and inner diameters of the nanofibers. As shown in Fig. 2**b** and Supplementary Fig. 4, the inner diameters of the hollow nanofibers increase from 0.33 ± 0.15 μm to 0.5 ± 0.11 μm and eventually reach 0.9 ± 0.16 μm, while the outer diameter remains constant at approximately 1.33 ± 0.15 μm. On such a basis, finite element analysis (FEA) was conducted to assess the acoustoelectric conversion performance of hollow nanofibers with different inner sizes under identical mechanical conditions, as illustrated in Fig. 2**c**. As the inner diameter increases, the overall vibration amplitude (Δx) increases gradually, correlating with the enhanced piezoelectric output. This phenomenon can be attributed to the thinner nanofiber wall, which lowers the bending stiffness of the nanofibers, making them more susceptible to strain (Fig. 2**d**)[42]. To further investigate the vibration behavior of hollow nanofibers under the acoustic field, the vibration characteristics of individual hollow nanofibers with varying inner sizes were analyzed across frequencies ranging from 0 to 800 Hz, as depicted in Fig. 2**e**. The results demonstrate that R3 exhibits the highest vibration amplitude compared to R0, R1, and R2. However, the piezoelectric output of nanofibers is not solely dependent on external excitation-induced deformation but is also related to the intrinsic material properties of the nanofibers, such as crystallinity and the β-phase content of PVDF, as demonstrated in our previous work [41]. Fig. 2**f** schematically shows the crystallization behavior of hollow nanofibers with different inner diameters. The crystallization sites can be systematically divided into outer layer crystallization sites (OCS) and inner core crystallization sites (ICS). With the inner size varied from R1 to R3, the number of ICS gradually increased due to the larger inner wall area, while the OCS remained constant due to the unchanged outer diameter. When the hollow nanofiber reaches a specific pore diameter, the ICS and OCS achieve a relative balance, resulting in peak crystallinity. Further increases in the inner diameter cause ICS and OCS to impinge and extrude each other, leading to a reduction in overall crystallinity (Fig. 2**g**). Therefore, an optimal inner diameter exists that maximizes the crystallinity of the hollow nanofibers, thereby enhancing the piezoelectric output. To validate the theoretical relationship between inner diameter and crystallinity, the composition and structure of these nanofibers were characterized by Fourier transform infrared spectrum (FTIR), X-ray diffraction (XRD), and differential scanning calorimetry (DSC). As shown in Fig. 2**h**, Supplementary Fig. 5, and Supplementary Notes 2–3**,** both crystallinity and melting temperature exhibit a pattern of initially increasing and subsequently decreasing as the inner diameter transitioned from R1 to R2 and then to R3. The observed trend in the melting temperature, as measured by DSC, can be attributed to the corresponding changes in crystallinity, where an initial increase in crystallinity leads to a higher melting temperature, followed by a decrease as crystallinity diminishes. Therefore, R2 demonstrates optimal performance based on these analyses. To further exclude the impact of PVP on PVDF crystallization behavior, molecular dynamics (MD) simulations were conducted on PVDF-PVP mixtures [43–46] (Fig. 2**i-j**, Supplementary Figs. 6-7). By comparing the conformations of molecular chains after 2 ns in pure PVDF and PVP/PVDF systems, the dihedral angle distributions (Gauche, Trans) of PVDF show no significant difference, with only a slight reduction in Trans in the PVP/PVDF system (Fig. 2**k**). This indicates that the introduction of PVP does not significantly alter the conformation of PVDF during the coaxial electrospinning. To experimentally validate the theoretical findings, the hollow nanofiber membrane was exposed to an acoustic source with frequencies

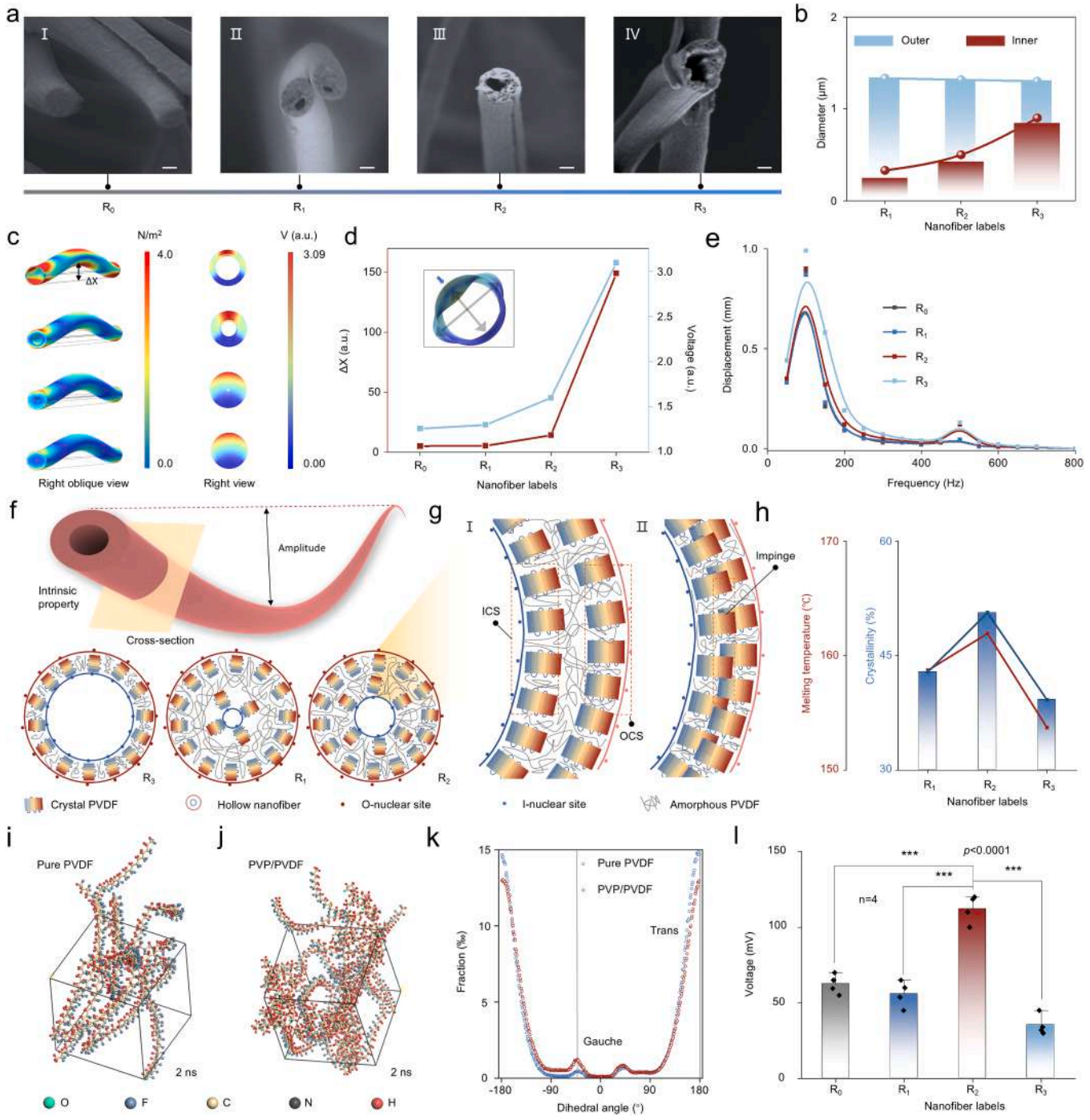


Fig. 2. Material characterization and analysis of hollow nanofibers. a SEM images of hollow nanofibers with different inner diameters. Scale bar is 0.5 μm; **b** Variation in outer and inner diameters of different hollow nanofibers; **c** FEA results showing the vibration (I) and voltage output (II) of hollow nanofiber with different inner diameters under identical forces. The color gradient from blue to red indicates increasing intensity; **d** FEA results of voltage and amplitude for hollow nanofibers, and the inset is a schematic of the structural deformation in nanofibers with an oversized inner diameter; **e** FEA results of the amplitude for nanofibers with different inner diameters at different frequencies; **f** Corresponding abstract models for crystal regions of nanofibers with different inner diameters; **g** Enlarged schematic of the crystal region, showing crystal balance (I) and crystal clash (II); **h** Melting temperature and crystallinity of R1, R2, R3; **i-j** Final snapshots from MD simulations of PVDF polymer with and without PVP; **k** Dihedral angles distributions of PVDF and PVP/PVDF chains near the 180° (Trans) and 60° (Gauche) averaged over the last 2 ns; **l** Voltage output intensity for nanofibers with different inner diameters under multiple measurement sweeps. Bar height, mean; error bars, s.d.; n = 4 independent samples.

ranging from 50 to 1000 Hz, and the corresponding piezoelectric voltage outputs were depicted in Supplementary Fig 8. All the hollow nanofiber membranes exhibit similar responses to acoustic waves. Notably, the R2 nanofibers demonstrate the highest piezoelectric voltage output, reaching up to 120 mV, significantly outperforming R0, R1, and R3, thus further substantiating the theory expounded in the previous section (Fig. 2**l** and Supplementary Note 4).

2.3. Acoustoelectric performance analysis of hollow nanofiber

To evaluate the specific acoustoelectric performance of the hollow nanofiber, we assembled a test platform wrapped with copper mesh to minimize external electromagnetic interference, thereby ensuring the accuracy and reliability of the experimental results (Fig. 3**a**, Supplementary Fig. 9, and Note 5). By definition, the SNR is the ratio of the strength of the received useful signal to the strength of the received noise signal, expressed by Eq. (1):

$$SNR = 20\lg\frac{V_s}{V_n} \tag{1}$$

where *Vs* and *Vn* are the voltage outputs of the HAS and the noise, respectively. As a result, the SNR of the HAS could reach as high as 290 ± 4.7 dB (Fig. 3**b** and Supplementary Fig. 10, and Note 6) [47]. The

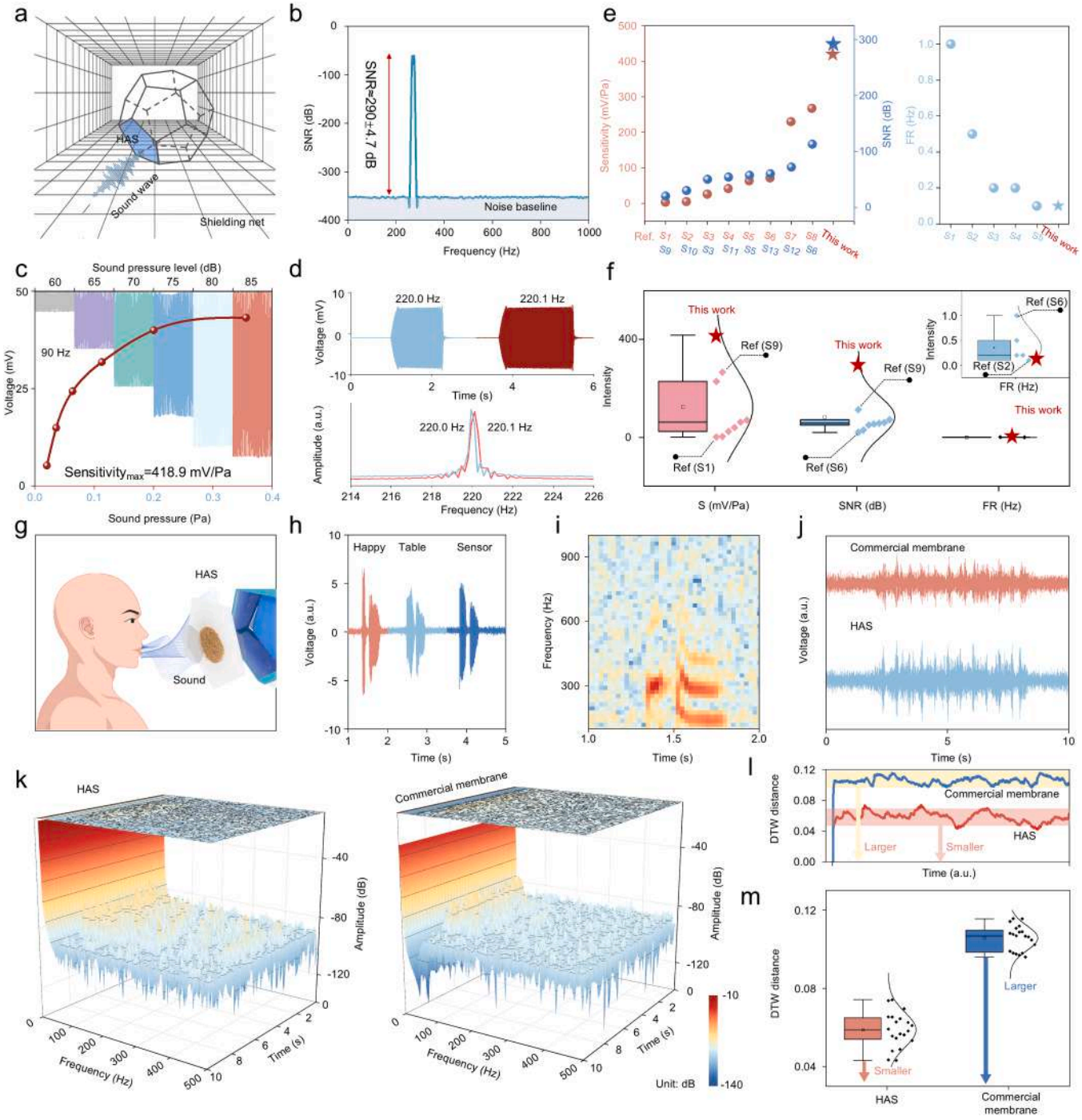


Fig. 3. Sound monitoring and signal analysis recorded by the HAS. a Schematic of the HAS test setup for acoustic wave detection; **b** SNR of the HAS at 270 Hz; **c** Voltage output and S of the HAS at 90 Hz under different sound pressures; **d** Voltage output and FFT spectrum of the HAS under acoustic stimulation with adjacent frequencies of 220 Hz and 220.1 Hz; **e-f** Comparison of *S*, SNR, and FR between the HAS with other reported acoustic sensors; **g** Schematic diagram of the HAS monitoring human voice; **h** Voltage output of words from human voice recorded by the HAS; **i** STFT spectrum of the word "Happy"; **j** Time-domain waveform comparison of signals recorded by the HAS and a commercial membrane; **k** 3D mapping of time domain, frequency domain, and amplitude of signals recorded by the HAS and a commercial membrane; **l-m** DTW analysis of 10 identical speech sequences recorded by the HAS and a commercial membrane.

sensitivity (S) is given by Eq. (2) :

$$S = \frac{V}{P} = \frac{V}{P_0 \times 10^{\frac{L_P}{20}}} \quad (2)$$

where P is the sound pressure, V is the voltage output of the HAS, P_0 is the reference sound pressure of 2×10^{-5} Pa, and L_P is the sound pressure level. As shown in Fig. 3**c**, the maximum S reaches 418 mV/Pa at 90 Hz. Additionally, the frequency resolution (FR) of the HAS achieves 0.1 Hz, even in noisy environments (Fig. 3**d,** Supplementary Fig. 11), further demonstrating its high-performance characteristics. Comparisons in terms of S, SNR, and FR indicate that the HAS (~418 mV/Pa, ~290 ± 4.7 dB) outperforms other sensors reported (~200 mV/Pa, ~80 dB, and ~0.5 Hz; ~48 mV/Pa, ~300 dB, and ~0.2 Hz of commercial membrane) across these metrics (Fig. 3**e-f** and Supplementary Fig. 12, Table 1). To demonstrate its practical applicability, the HAS was employed for human voice monitoring (Fig. 3**g**). From the recording results for different words ("Happy", "Table", and "Sensor"), it is clear

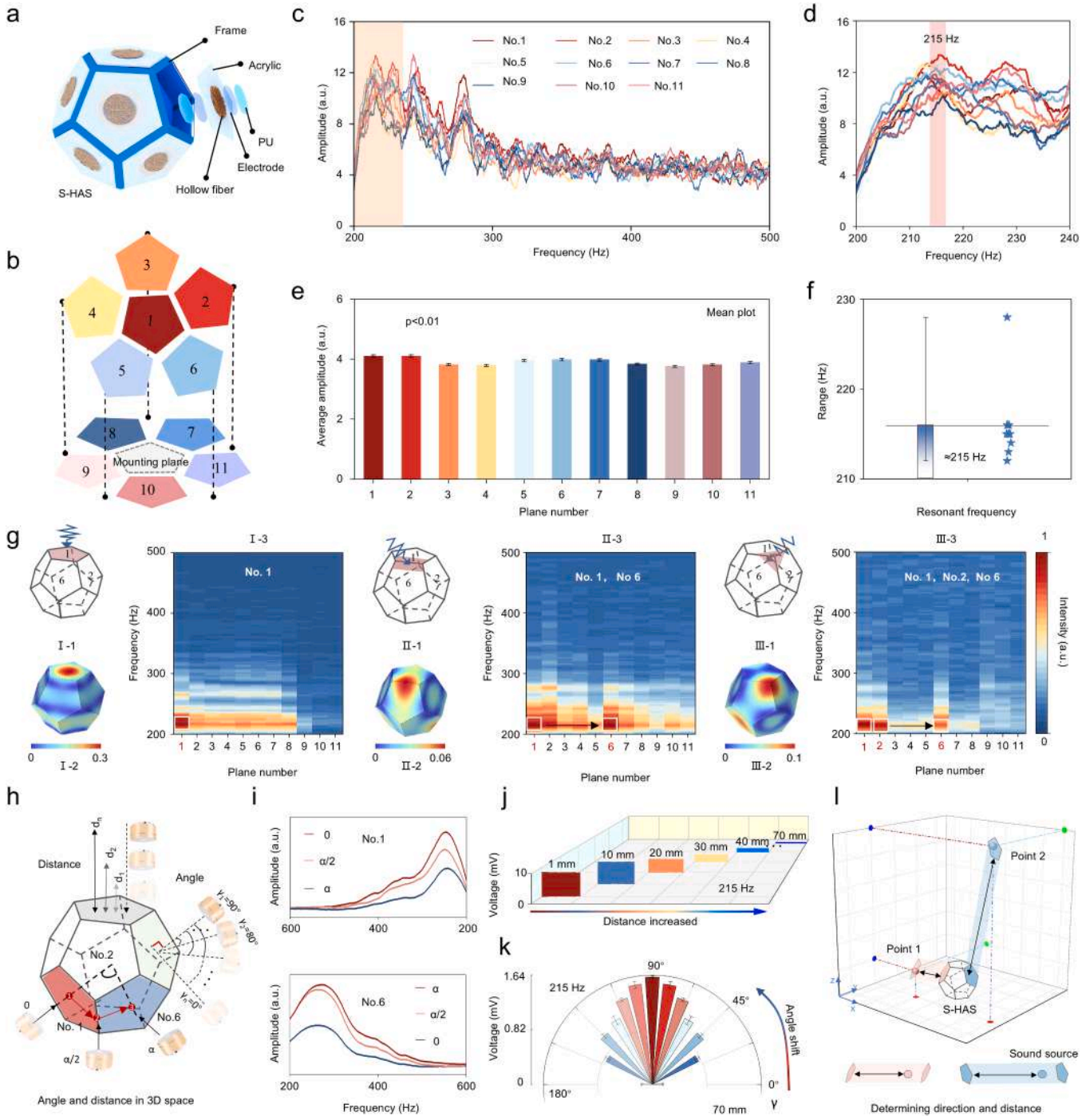


Fig. 4. Design of S-HAS and its application in sound localization. a Schematic diagram of S-HAS; **b** Schematic of the unfolded faces of the S-HAS; **c** Vibration amplitude of each face of S-HAS under acoustic frequencies ranging from 200 to 500 Hz; **d** Enlarged view of vibration amplitude for frequencies during 200–240 Hz; **e** Statistical analysis of the average vibration amplitude of different planes; **f** Statistical analysis of the response of 11 functional layers at 215 Hz; **g** Signal mapping of the S-HAS for 200–500 Hz sound at different incident directions. The white wireframe indicates that the plane has the strongest response; **h-k** Test schematic and electrical output of the S-HAS under varying sound source distances and angles; **l** Demonstration of the 3D spatial positioning.

that the HAS exhibits differentiated signal characteristics for each word, as evidenced by the time domain waveforms, fast Fourier transform (FFT) spectra, and short-time Fourier transforms (STFT) spectra (Fig. 3**h-i**, Supplementary Figs. 13-14 and Movie 1).

Additionally, the HAS demonstrates superior acoustic capture capabilities, successfully recording both complex sentences (Supplementary Fig. 15 and Movie 2) and faint heart sounds (Supplementary Note 7), which highlights its capability to monitor complex auditory signals. To further validate the authenticity and reliability of the recorded results, we compared the same audio segment captured by the HAS and a commercial membrane (Fig. 3**j** and Supplementary Fig. 16). The comparison results show a clear correspondence between the characteristic peaks of the two time-domain signals. Notably, the 3D mapping shows that the amplitude of the signal recorded by the HAS is higher than that of the commercial membrane across all frequency bands (Fig. 3**k**). Dynamic time warping (DTW) algorithms are employed to evaluate the similarity of different speech signals [48]. We analyzed 10 identical speech sequences recorded by the HAS and the commercial membrane, with the HAS consistently outperforming the commercial membrane in DTW analysis (Fig. 3**l**). Further quantitative statistics show that the DTW of the HAS is about 0.06, which is only 54% of that of the commercial membrane (Fig. 3**m**). The smaller and more focused DTW distances indicate that the waveforms recorded by the HAS are more stable and reliable, providing robust support for sound discrimination.

2.4. Sound localization and identification based on S-HAS

Spatial sound localization is critical in acoustic electronics, particularly for advancing acoustic sensing and human-machine interface (HMI) applications. To address this gap, we integrated HAS into a multi-directional sphere (S-HAS), enabling sound recognition and localization in 3D space (Fig. 4**a,** Supplementary Fig. 17, and Note 8), including the assembled S-HAS, the constituent frames, and individual units, respectively. To better understand the composition of the S-HAS and the interrelationships between its working surfaces, the S-HAS is dissected, as shown in Fig. 4**b**. The S-HAS adopts an ortho dodecahedral structure, comprising eleven surfaces dedicated to acoustic sensing and one plane for wire mounting. The top plane opposite the mounting surface is designated as plane No.1, while planes No.2 to No.6 are adjacent to plane No.1. Similarly, plane No.2 is laterally adjacent to planes No.7 and No.11, forming an interconnected edge structure. Fig. 4**c** and Supplementary Fig. 18 show that all the acoustic sensing planes of the S-HAS exhibit highly consistent responses to normal incident sound waves across frequencies spanning from 200 to 1000 Hz. As can be seen from the amplified response for frequencies between 200 Hz and 240 Hz**,** each plane displays a uniform output response, with a distinct peak observed at approximately 215 Hz (Fig. 4**d**). Statistical analysis further confirms the consistency of these average responses, with a *p*-value of less than 0.01 (Fig. 4**e-f**). Different incidence angles and distances yield distinct acoustic responses, allowing S-HAS to realize 3D spatial sound localization. Fig. 4**g** and Supplementary Fig. 19 present the three angular resolution modes of S-HAS: vertical incidence (VI), double-sided line incidence (DI), and three-sided line incidence (TI). In VI mode, when sound waves are incident perpendicularly on plane No.1, this surface exhibits the largest vibration amplitude (Fig. 4g-I−1, 4g-I−2), while other surfaces vibrate less due to attenuated air-induced oscillations, as shown in the vibration thermogram (Fig. 4g-I−3). When the sound wave incidence changes from VI to DI mode (Fig. 4g-II−1, 4g-II−2), significant changes are observed in the vibration surfaces (Fig. 4g-II−3). Planes No.1 and No.6 exhibit larger amplitudes along their edges than other planes. Similarly, in TI mode, the three surfaces (planes No.1, No.2, and No.6) sharing a common vertex exhibit larger amplitudes than the others. Therefore, these relative amplitude intensities can serve as criteria for sound source localization. The angle and distance of the sound source are also key indicators for positioning (Fig. 4**h**). When the sound source moves from perpendicular incidence to plane No.1 (0°), to α/2, and then to plane No.6 (α) along the circumference (where α is the 63° angle between neighboring planes), the measured spectra show a gradual decrease in the amplitude intensity on plane No.1 and a corresponding increase on plane No.6, indicating that the S-HAS can discriminate the sound sources from different angles (Fig. 4**i,** Supplementary Figs. 20–21). Furthermore, we also investigated the response of a single-sided membrane of S-HAS to a sound source at different angles and distances, as depicted in Fig. 4**j**. The voltage output of the S-HAS increases gradually as the sound source distance decreases from 70 mm to 1 mm. Similarly, the voltage output varies in response to gradual changes in the sounding incidence angle, shifting from 90° (perpendicular to the device plane) to 0° (parallel to the device) (Fig. 4**k**, Supplementary Fig. 22). Notably, the S-HAS maintains its ability to distinguish these changes effectively, demonstrating a minimum angular resolution as low as 10°, thanks to the efficient segmentation of spatial homogeneity by S-HAS and the high performance of its hollow nanofibers. Therefore, when an acoustic source is placed at any point in 3D space, the S-HAS is capable of accurately localizing it (Fig. 4**l**, Supplementary Fig. 23). This capability overcomes the limitations of conventional devices that can only respond to unidirectional acoustic waves and significantly improves spatial acoustic localization.

2.5. Intelligent binaural auditory system based on S-HAS

The developed S-HAS mimics the binaural auditory system, enabling precise sound recognition and localization for HMI with the assistance of deep learning algorithms (Fig. 5**a-c**). This innovation holds promise for expanding the application scope of next-generation auditory devices, enabling more humanized and intelligent functionalities (Fig. 5**d**). As a proof-of-concept, we recorded the voices "Who is talking?" from six different volunteers using the S-HAS, with the corresponding time-domain waveforms presented in Fig. 5**e**. To analyze the high-dimensional data, we employed the t-distributed stochastic neighborhood embedding (t-SNE) technique to map them into a low-dimensional space, followed by K-means clustering for pattern identification. The resulting visualization demonstrates that data points belonging to distinct categories form well-separated clusters, displaying enhanced discriminative features compared to the original data. This approach facilitates the effective identification and clustering of individual voices (Fig. 5**f**). To achieve accurate voice recognition, we constructed a 1D-CNN algorithm comprising multiple processing layers. Each layer progressively learns deeper features, effectively filtering out invalid data and amplifying valid information. This process enhances the accuracy and interpretability of the extracted features, making the CNN highly suitable for processing acoustic signals. We conducted multiple rounds of acoustic signal acquisition from several volunteers and randomly divided the entire dataset into training, validation, and test sets in a ratio of 7:2:1 [43]. Fig. 5**g** illustrates the variation in training and testing accuracies, with the highest accuracy reached at the 20th iteration, indicating that the proposed model can achieve high classification accuracy and robustness. For comparison, the same CNN parameters were used to train, validate, and test voice information recorded by the commercial membrane. The testing accuracy of S-HAS is consistently higher and more stable than that of the commercial membrane, highlighting its superior performance (Fig. 5**h** and Supplementary Figs. 24–25). Additionally, Fig. 5**i-j** display the confusion matrices of predicted and actual labels in the test set after 100 training epochs for both the S-HAS and the commercial membrane. The developed S-HAS system demonstrates an average prediction accuracy of 98.83%, significantly surpassing 93.89% of the commercial membrane. This superior performance is attributed to the high sensitivity, excellent SNR, and superior frequency resolution of the hollow nanofibers in the S-HAS. These advantages enable the S-HAS to capture more detailed voice information during acoustic signal acquisition, facilitating more effective feature learning. In addition, the developed S-HAS system demonstrates

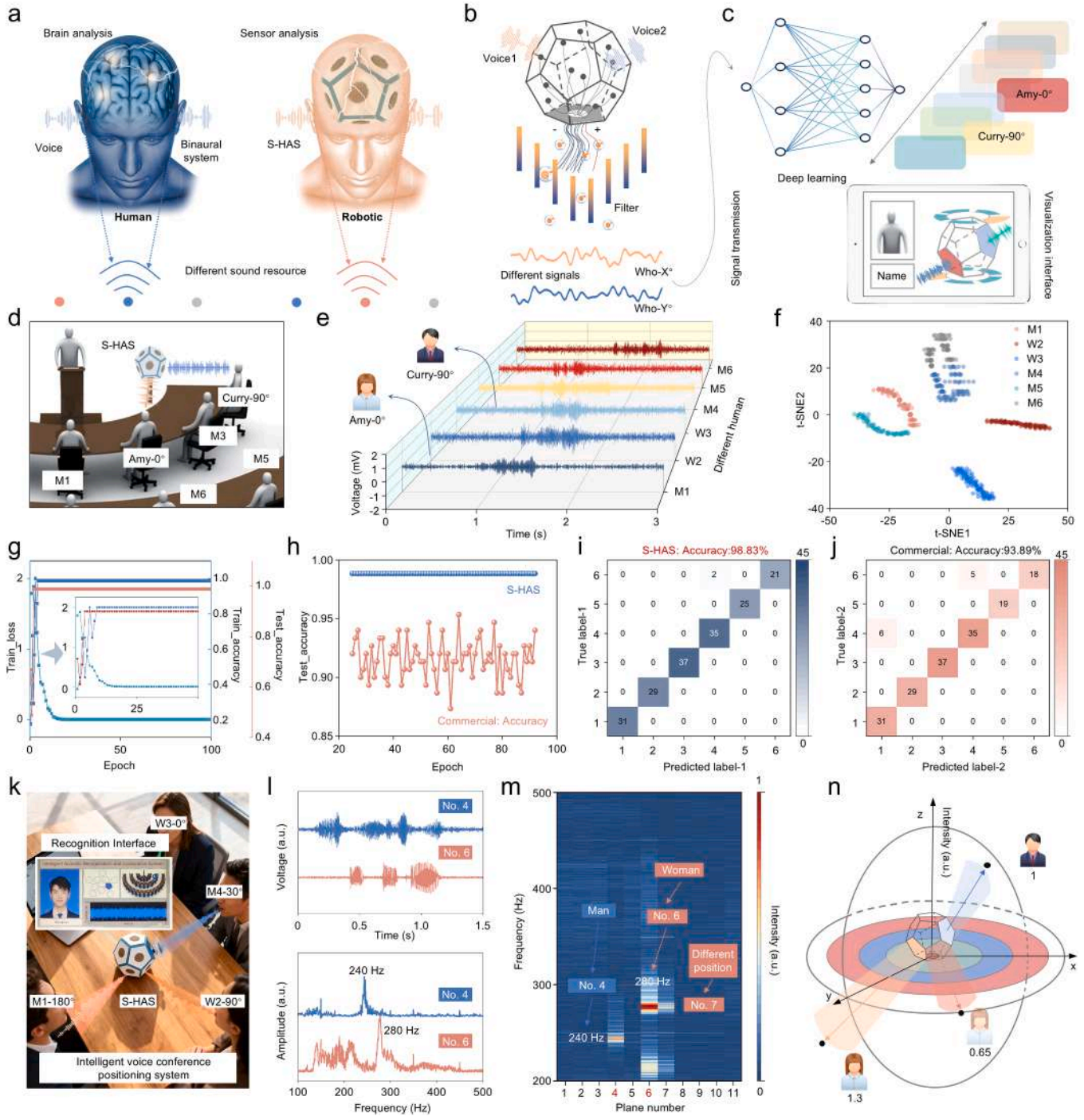


Fig. 5. S-HAS intelligent binaural auditory for sound recognition and localization. a-c Comparison of binaural localization recognition in humans and S-HAS; **d** Acoustic sensing scenario with multi-angle and multi-source sound detection; **e** Time-domain of the sentence "Who is talking?" recorded from six different individuals using the S-HAS; **f** Visualization of the output data by K-mean clustering after dimensionality reduction via t-SNE; **g** Evaluation of the classification accuracy, training accuracy, and loss function over 100 epochs; **h** Comparison of testing accuracy between the S-HAS and the commercial membrane after 25 epochs; **i-j** Confusion matrices comparing the S-HAS and the commercial membrane for sound recognition; **k** Schematic diagram of different individuals speaking to the S-HAS from different angles; **l** Time-domain and frequency-domain signals of the sentence "Who is talking?"; **m** Frequency intensity mapping across different planes of the S-HAS; **n** Schematic diagram of angle detection and recognition display.

great potential for omnidirectional sound localization, a key capability for next-generation intelligent robotic applications. Experimental validation using spatially distributed sound sources confirms the system's adaptability and spatial resolution. Fig. 5**k-l** shows that the S-HAS recorded voices from two individuals positioned in different directions. The frequency of the male voice is concentrated at 240 Hz, while the female voice is concentrated at 280 Hz (Supplementary Figs. 26–27). The highest frequency intensities (240 Hz and 280 Hz) are found in planes No.4 and No.6, respectively (Fig. 5**m**). This allows us to locate the male speaker in the direction corresponding to plane No.4 and the female speaker in the direction corresponding to plane No.6, and it also allows us to locate the female speaker in different distances based on amplitude intensity thus realizing the sound localization, thus realizing the sound localization (Fig. 5**n**, Supplementary Figs. 28–29, and Movie

3). These capabilities position the S-HAS as a promising candidate for advancing HMI systems, with potential applications in bionic hearing and intelligent voice authentication.

3. Conclusion

In summary, we developed a hollow-structured piezoelectric nanofiber acoustic system that establishes an effective strategy for synergistically regulating the crystallization behavior and acoustic interaction of PVDF. Through hollow structural engineering, the acoustic responsiveness and signal fidelity of the piezoelectric sensor were significantly enhanced, enabling high-performance sound sensing and spatial acoustic perception. Moreover, the S-HAS demonstrated reliable omnidirectional sound recognition and localization capabilities, highlighting the feasibility of combining structural acoustics with piezoelectric bioelectronics. This work not only provides new insights into hollow collaborative regulation mechanisms in piezoelectric materials but also offers a scalable and adaptable platform for next-generation intelligent acoustic sensing and human–machine interaction systems.

4. Materials and methods

4.1. Preparation of solutions and materials

First, 1.84 g of PVDF (MW~180,000 g/mol, Sigma Aldrich) and 1 g of PVP (MW~58,000 g/mol, K29–32, Aladdin) were dissolved in 5 mL of a mixed solvent consisting of 3.25 mL of N-N-dimethylacetamide (Sigma Aldrich) and 1.75 mL of acetone (Sigma Aldrich). The mixture was heated and stirred in a water bath at 60°C for 2 h to obtain a bubble-free, uniform mixture for preparing the shell layer of the hollow nanofibers. Then, another mixture with different concentrations (10%, 20%, and 30%) of PVP (MW~1300,000 g/mol, K88–96, Aladdin) was dissolved in 5 mL of anhydrous ethanol, and stirred for 60 min to prepare the core layer of the hollow nanofibers.

4.2. Electrospinning process and fabrication of the hollow nanofiber

Coaxial electrospinning was performed using a 22/17-gauge blunt-end coaxial stainless steel needle. The feed rates of the inner (core) and outer (shell) layer solutions were 0.5 mL/h and 0.4 mL/h, respectively. The needle was connected to a high-voltage supply at 14 ± 1 kV, and the PVDF/PVP nanofibers were collected using a drum collector covered with aluminum foil rotating at 1000 rpm. The receiving plate was kept at a distance of 10.5 ± 1 cm from the needle, and the electrospinning was conducted for 2 h under ambient conditions (25 °C and 50% humidity). Then, the resulting nanofibers were placed in an oven at 60 °C for 12 h. After annealing, the nanofibers were placed in an anhydrous ethanol solution and sonicated for 2 h to remove the PVP to obtain hollow nanofibers. Then, silver electrodes were deposited onto the hollow nanofiber membrane via magnetron sputtering for 10 min, and the electrodes were connected with copper wires in the same manner as reported in previous work [43].

4.3. FEA and vibration detection

The FEA was employed to analyze the vibration modes and piezoelectric outputs of the hollow nanofibers with different inner diameters. The microscale electrospinning piezoelectric membrane network was simplified as a PVDF membrane with a Young's modulus of 840 MPa and a Poisson's ratio of 0.4. The vibrational modes were simulated under a single force for nanofibers with different inner diameters (The specific values were shown in Supplementary Table 2). Acoustic signals ranging from 50 to 800 Hz were used to stimulate the nanofibers with different inner diameters to obtain their vibration modes under acoustic fields. A 12-plane model was constructed, with each plane assigned a Young's modulus of 840 MPa and a Poisson's ratio of 0.4 for the PVDF membrane. The single-point source with a power of 500 W and a frequency range of 50–800 Hz was applied. All simulations were performed by commercial software (COMSOL Multiphysics 6.0).

4.4. Molecular dynamics (MD) simulations

MD simulations were conducted using six PVDF molecules (each containing 40 VDF monomers) and four PVP molecules (each containing 20 NVP monomers), with an initial density of 1.1 g/cm^3 , corresponding to the polymer concentrations of PVP/PVDF. The COMPASS II Force Field was employed to describe the intra- and intermolecular interactions of the PVDF and PVP chains. For equilibration, both the pure PVDF model and the PVP/PVDF model were initially geometry-optimized and energy-minimized. These models were then equilibrated using the NVT ensemble (constant number of atoms, volume, and energy) at 298 K under an electric field of 1 V/nm for 2.0 ns. Newton's equations of motion were integrated using the velocity-Verlet algorithm with a time step of 1 fs. The temperature and distribution of atomic velocities in the system were related through the Maxwell-Boltzmann distribution. Van der Waals and electrostatic interactions were considered in both models, with a cut-off distance of 15.5 Å for non-bonded interactions. All MD simulations were conducted using Materials Studio 2020.

4.5. Materials characterization and electrical performance measurement

The morphologies of hollow nanofiber and PVP were studied by field-emission scanning electron microscopy (FESEM, JSM-7800f). The crystal content and phase structure of the PVDF, PVP, and their composites were determined by Raman spectroscopy (HORIBA JobinYvon XploRA ONE, 532 nm laser), differential scanning calorimetry (DSC, Mettler Toledo), X-ray diffraction (XRD, X PERT MPD Pro), and Fourier-transform infrared spectroscopy (FTIR, Nicolet 5700 Spectrometer). Then, the voltage output of the HAS and S-HAS was recorded by a Keithley−6514 electrometer, and the signal was collected and analyzed by a data acquisition card (NI PCI−6221). A commercial PVDF piezoelectric membrane (Model CZ3460, TE/PolyK, USA) with a thickness of 52 μm, d33 of −26 pC/N, Young's modulus of 2.2–2.8 × 109 N/m2, and electromechanical coupling coefficient of 10~13% was used for comparison.

4.6. K-means clustering using t-SNE and deep learning for sound recognition

Voice samples of six volunteers were collected with the S-HAS, with 100 samples per volunteer (600 total samples) and 6000 data points per sample. t-SNE was used for data dimensionality reduction, where random state, init, learning rate, and perplexity of t-SNE were 42, random, 500, and 30, respectively. K-means clustering was applied to categorize different voice signals. Then, a three-layer 1D-CNN was constructed for data feature extraction and automatic recognition of voice signals. Voice data from six volunteers was collected using both the S-HAS and the commercial membrane, with each sound recorded 10 times (4000 data points per recording). The dataset was augmented eightfold and randomly split into a training set, a validation set, and a test set in the ratio of 7:2:1. The model was trained with 70% of the data, validated on 20%, and tested on the remaining 10%. Classification accuracy, learning rate, and loss function were evaluated during each training epoch to optimize the model.

4.7. Statistical analysis

Multiple measurements were conducted to ensure the robustness of the experimental conclusions and mitigate potential confounding factors. One-way ANOVA was employed for statistical analysis. All the experiments were performed in triplicate. The obtained data were

expressed as the mean value ± standard deviation. All data processing was conducted using Origin software.

CRediT authorship contribution statement

Boling Lan: Writing – review & editing, Writing – original draft, Visualization, Validation, Supervision, Software, Resources, Methodology, Investigation, Formal analysis, Data curation, Conceptualization. **Yong Ao:** Formal analysis. **Yue Sun:** Investigation. **Guo Tian:** Validation, Software, Formal analysis. **Tao Yang:** Software, Investigation. **Shenglong Wang:** Software. **Longchao Huang:** Validation. **Tingting Zhou:** Visualization. **Peiwen Li:** Data curation. **Zihan Wang:** Software. **Tianpei Xu:** Software. **Guicen Liu:** Software. **Jinlong Sun:** Software. **Hongguang Li:** Resources. **Long Jin:** Visualization, Software. **Binbin Zhang:** Validation, Software. **Fengjun Chun:** Software, Formal analysis. **Weili Deng:** Writing – review & editing, Writing – original draft, Visualization, Validation, Supervision, Funding acquisition. **Weiqing Yang:** Writing – review & editing, Writing – original draft, Visualization, Funding acquisition.

Declaration of Competing Interest

The authors declare no conflicts of interest.

Acknowledgments

This work was supported by the National Natural Science Foundation of China (Grant No. U2330120) and the Basic Research Cultivation Project of Southwest Jiaotong University (Grant No. 2682023KJ024). All testing involving human participants is approved by the Institutional Review Boards of Southwest Jiaotong University with the reference number of SWJTU−23012-NSFC(133). Informed consent was obtained from all volunteers before enrollment in this study. We are thankful for the help from the Analysis and Testing Center of Southwest Jiaotong University.

Reporting summary

Further information on research design is available in the Nature Portfolio Reporting Summary linked to this article.

Appendix A. Supporting information

Supplementary data associated with this article can be found in the online version at doi:10.1016/j.nanoen.2026.112122.

Data availability

Data will be made available on request.

References

[1] S. Prameela, T. Pollock, D. Raabe, M. Meyers, A. Aitkaliyeva, K. Chintersingh, Z. Cordero, L. Graham-Brady, Materials for extreme environments, Nat. Rev. Mater. 8 (2023) 81–88, https://doi.org/10.1038/s41578-022-00496-z.
[2] M. Ortiz-Catalan, J. Zbinden, J. Millenaar, D. D'Accolti, M. Controzzi, F. Clemente, L. Cappello, E. Earley, E. Mastinu, J. Kolankowska, M. Munoz-Novoa, S. Jönsson, C. Cipriani, P. Sassu, R. Brånemark, A highly integrated bionic hand with neural control and feedback for use in daily life, Sci. Robot. 8 (2023) eadf7360, https://doi.org/10.1126/scirobotics.adf7360.
[3] P. Dupont, B. Nelson, M. Goldfarb, B. Hannaford, A. Menciassi, M. O'Malley, N. Simaan, P. Valdastri, G. Yang, A decade retrospective of medical robotics research from 2010 to 2020, Sci. Robot. 6 (2021) eabi8017, https://doi.org/10.1126/scirobotics.abi8017.
[4] D. Zhong, C. Wu, Y. Jiang, Y. Yuan, M. Kim, Y. Nishio, C. Shih, W. Wang, J. Lai, X. Ji, T. Gao, Y. Wang, C. Xu, Y. Zheng, Z. Yu, H. Gong, N. Matsuhisa, C. Zhao, Y. Lei, D. Liu, S. Zhang, Y. Ochiai, S. Liu, S. Wei, J. Tok, Z. Bao, High-speed and large-scale intrinsically stretchable integrated circuits, Nature 627 (2024) 313–320, https://doi.org/10.1038/s41586-024-07096-7.
[5] B. Zhang, J. Li, J. Zhou, L. Chow, G. Zhao, Y. Huang, Z. Ma, Q. Zhang, Y. Yang, C. Yiu, J. Li, F. Chun, X. Huang, Y. Gao, P. Wu, S. Jia, H. Li, D. Li, Y. Liu, K. Yao, R. Shi, Z. Chen, B. Khoo, W. Yang, F. Wang, Z. Zheng, Z. Wang, X. Yu, A three-dimensional liquid diode for soft, integrated permeable electronics, Nature 628 (2024) 84–92, https://doi.org/10.1038/s41586-024-07161-1.
[6] J. Yin, S. Wang, T. Tat, J. Chen, Motion artefact management for soft bioelectronics, Nat. Rev. Bioeng. 2 (2024) 541–558, https://doi.org/10.1038/s44222-024-00175-4.
[7] Z. Yan, D. Xu, Z. Lin, P. Wang, B. Cao, H. Ren, F. Song, C. Wan, L. Wang, J. Zhou, X. Zhao, J. Chen, Y. Huang, X. Duan, Highly stretchable van der Waals thin films for adaptable and breathable electronic membranes, Science 375 (2022) 852–859, https://doi.org/10.1126/science.abl8941.
[8] Y. Wang, C. Sun, D. Ahmed, A smart acoustic textile for health monitoring, Nat. Electron. 8 (2025) 485–495, https://doi.org/10.1038/s41928-025-01386-2.
[9] S. Zhang, Y. Zhou, A. Libanori, Y. Deng, M. Liu, M. Zhou, H. Qu, X. Zhao, P. Zheng, Y. Zhu, S. Tan, J. Chen, Biomimetic spinning of soft functional fibres via spontaneous phase separation, Nat. Electron. 6 (2023) 338–348, https://doi.org/10.1038/s41928-023-00960-w.
[10] Z. Shen, D. Zhu, M. Zhang, Synergy of smart materials and structures toward intelligent metamaterials, Smartsys 1 (2025) e70007, https://doi.org/10.1002/sys3.70007.
[11] B. Shao, T. Wu, Z. Yan, T. Ko, W. Peng, D. Jhan, Y. Chang, J. Fong, M. Lu, W. Yang, J. Chen, M. Lu, B. Sun, H. Liu, R. Liu, Y. Lai, Deep learning–empowered triboelectric acoustic textile for voice perception and intuitive generative AI-voice access on clothing, Sci. Adv. 11 (2025) eadx3348, https://doi.org/10.1126/sciadv.adx3348.
[12] S. Gong, X. Zhang, X. Nguyen, Q. Shi, F. Lin, S. Chauhan, Z. Ge, W. Cheng, Hierarchically resistive skins as specific and multimetric on-throat wearable biosensors, Nat. Nanotechnol. 18 (2023) 889–897, https://doi.org/10.1038/s41565-023-01383-6.
[13] Y. Xu, E. Paz, A. Paul, K. Mahato, J. Sempionatto, N. Tostado, M. Lee, G. Hota, M. Lin, A. Uppal, W. Chen, S. Dua, L. Yin, B. Wuerstle, S. Deiss, P. Mercier, S. Xu, J. Wang, G. Cauwenberghs, In-ear integrated sensor array for the continuous monitoring of brain activity and of lactate in sweat, Nat. Biomed. Eng. 7 (2023) 1307–1320, https://doi.org/10.1038/s41551-023-01095-1.
[14] J. Chang, T. Maltby, A. Moineddini, D. Shi, L. Wu, J. Chen, J. Yu, J. Hung, G. Viola, A. Vilches, W. Song, Piezoelectric nanofiber–based intelligent hearing system, Sci. Adv. 11 (2025) eadl2741, https://doi.org/10.1126/sciadv.adl2741.
[15] Z. Zhou, K. Chen, X. Li, S. Zhang, Y. Wu, Y. Zhou, K. Meng, C. Sun, Q. He, W. Fan, E. Fan, Z. Lin, X. Tan, W. Deng, Jin Yang, J. Chen, Sign-to-speech translation using machine-learning-assisted stretchable sensor arrays, Nat. Electron. 3 (2020) 571–578, https://doi.org/10.1038/s41928-020-0428-6.
[16] X. Zhao, Y. Zhou, A. Li, J. Xu, S. Karjagi, E. Hahm, L. Rulloda, J. Li, J. Hollister, P. Kavehpour, J. Chen, A self-filtering liquid acoustic sensor for voice recognition, Nat. Electron. 7 (2024) 924–932, https://doi.org/10.1038/s41928-024-01196-y.
[17] H. Lee, J. Chung, G. Hwang, C. Jeong, Y. Jung, J. Kwak, H. Kang, M. Byun, W. Kim, S. Hur, S. Oh, K. Lee, Flexible inorganic piezoelectric acoustic nanosensors for biomimetic artificial hair cells, Adv. Funct. Mater. 24 (2014) 6914–6921, https://doi.org/10.1002/adfm.201402270.
[18] T. Le, J. An, Y. Huang, Q. Vo, J. Boonruangkan, T. Tran, S. Kim, G. Sun, Y. Kim, Ultrasensitive anti-interference voice recognition by bio-inspired skin-attachable self-cleaning acoustic sensors, ACS Nano 13 (2019) 13293–13303, https://doi.org/10.1021/acsnano.9b06354.
[19] Z. Wang, N. Shi, Y. Zhang, N. Zheng, H. Li, Y. Jiao, J. Cheng, Y. Wang, X. Zhang, Y. Chen, Y. Chen, H. Wang, T. Xie, Y. Wang, Y. Ma, X. Gao, X. Feng, Conformal in-ear bioelectronics for visual and auditory brain-computer interfaces, Nat. Commun. 14 (2023) 4213, https://doi.org/10.1038/s41467-023-39814-6.
[20] W. Yan, G. Noel, G. Loke, E. Meiklejohn, T. Khudiyev, J. Marion, G. Rui, J. Lin, J. Cherston, A. Sahasrabudhe, J. Wilbert, I. Wicaksono, R. Hoyt, A. Missakian, L. Zhu, C. Ma, J. Joannopoulos, Y. Fink, Single fibre enables acoustic fabrics via nanometre-scale vibrations, Nature 603 (2022) 616–623, https://doi.org/10.1038/s41586-022-04476-9.
[21] H. Xu, W. Zheng, Y. Zhang, D. Zhao, L. Wang, Y. Zhao, W. Wang, Y. Yuan, J. Zhang, Z. Huo, Y. Wang, N. Zhao, Y. Qin, K. Liu, R. Xi, G. Chen, H. Zhang, C. Tang, J. Yan, Q. Ge, H. Cheng, Y. Lu, L. Gao, A fully integrated, standalone stretchable device platform with in-sensor adaptive machine learning for rehabilitation, Nat. Commun. 14 (2023) 7769, https://doi.org/10.1038/s41467-023-43664-7.
[22] N. Meng, X. Ren, G. Santagiuliana, L. Ventura, H. Zhang, J. Wu, H. Yan, M. Reece, E. Bilotti, Ultrahigh beta-phase content poly(vinylidene fluoride) with relaxor-like ferroelectricity for high energy density capacitors, Nat. Commun. 10 (2019) 4535, https://doi.org/10.1038/s41467-019-12391-3.
[23] W. Deng, Y. Zhou, A. Libanori, G. Chen, W. Yang, J. Chen, Piezoelectric nanogenerators for personalized healthcare, Chem. Soc. Rev. 51 (2022) 3317–3820, https://doi.org/10.1039/d1cs00858g.
[24] T. Su, N. Liu, D. Lei, L. Wang, Z. Ren, Q. Zhang, J. Su, Z. Zhang, Y. Gao, Flexible MXene/bacterial cellulose film sound detector based on piezoresistive sensing mechanism, ACS Nano 16 (2022) 8461–8471, https://doi.org/10.1021/acsnano.2c03155.
[25] G. Gou, X. Li, J. Jian, H. Tian, F. Wu, J. Ren, X. Geng, J. Xu, Y. Qiao, Z. Yan, G. Dun, C. Ahn, Y. Yang, T. Ren, Two-stage amplification of an ultrasensitive MXene-based intelligent artificial eardrum, Sci. Adv. 8 (2022) eabn2156, https://doi.org/10.1126/sciadv.abn2156.
[26] J. Liu, G. Tian, W. Yang, W. Deng, Recent progress in flexible piezoelectric devices toward human-machine interactions, Soft Sci. 2 (2022) 22, https://doi.org/10.20517/ss.2022.23.

[27] Y. Zhang, X. Zhou, N. Zhang, J. Zhu, N. Bai, X. Hou, T. Sun, G. Li, L. Zhao, Y. Chen, L. Wang, C. Guo, Ultrafast piezocapacitive soft pressure sensors with over 10 kHz bandwidth via bonded microstructured interfaces, Nat. Commun. 15 (2024) 3048, https://doi.org/10.1038/s41467-024-47408-z.
[28] J. Xia, H. Lu, G. Chen, D. Lin, W. Yang, C. Liu, B. Hu, Y. Zhao, High performance piezoelectric nanogenerator by fiber microstructure engineering toward self-powered wireless sensing system, Nano Energy 128 (2024) 109901, https://doi.org/10.1016/j.nanoen.2024.109901.
[29] H. Lu, Z. Hu, X. Wang, G. Chen, X. Zheng, J. Xia, M. Huang, W. Yang, J. Liu, B. Hu, J. Adv. Ceram. 14 (2025) 9221171, https://doi.org/10.26599/JAC.2025.9221171.
[30] H. Guo, X. Pu, J. Chen, Y. Meng, M. Yeh, G. Liu, Q. Tang, B. Chen, D. Liu, S. Qi, C. Wu, C. Hu, J. Wang, Z. Wang, A highly sensitive, self-powered triboelectric auditory sensor for social robotics and hearing aids, Sci. Robot. 3 (2018) eaat2516, https://doi.org/10.1126/scirobotics.aat2516.
[31] S. Lee, J. Kim, I. Yun, G. Bae, D. Kim, S. Park, I. Yi, W. Moon, Y. Chung, K. Cho, An ultrathin conformable vibration-responsive electronic skin for quantitative vocal recognition, Nat. Commun. 10 (2019) 2468, https://doi.org/10.1038/s41467-019-10465-w.
[32] H. Tang, S. Zhang, Y. Tian, T. Kang, C. Zhou, S. Yang, Y. Liu, X. Liu, Q. Chen, H. Xiao, W. Chen, J. Zang, Bioinspired soft elastic metamaterials for reconstruction of natural hearing, Adv. Sci. 10 (2023) 2207273, https://doi.org/10.1002/advs.202207273.
[33] Z. Che, X. Wan, J. Xu, C. Duan, T. Zheng, J. Chen, Speaking without vocal folds using a machine-learning-assisted wearable sensing-actuation system, Nat. Commun. 15 (2024) 1873, https://doi.org/10.1038/s41467-024-45915-7.
[34] H. Wang, S. Hong, J. Han, Y. Jung, H. Jeong, T. Im, C. Jeong, B. Lee, G. Kim, C. Yoo, K. Lee, Biomimetic and flexible piezoelectric mobile acoustic sensors with multiresonant ultrathin structures for machine learning biometrics, Sci. Adv. 7 (2021) eabe5683, https://doi.org/10.1126/sciadv.abe5683.
[35] A. Silva, P. Sahoo, A. Cavalli, A. de Souza, E. Bakkers, C. Cesar, R. Janissen, M. Cotta, Nanowire arrays as force sensors with super-resolved localization position detection: application to optical measurement of bacterial adhesion forces, Small Methods 2 (2018) 1700411, https://doi.org/10.1002/smtd.201700411.
[36] H. Shao, H. Wang, Y. Cao, X. Ding, R. Bai, H. Chang, J. Fang, X. Jin, W. Wang, T. Lin, Single-layer piezoelectric nanofiber membrane with substantially enhanced noise-to-electricity conversion from endogenous triboelectricity, Nano Energy 89 (2021) 106427, https://doi.org/10.1016/j.nanoen.2021.106427.
[37] J. Li, C. Carlos, H. Zhou, J. Sui, Y. Wang, Z. Silva-Pedraza, F. Yang, Y. Dong, Z. Zhang, T. Hacker, B. Liu, Y. Mao, X. Wang, Stretchable piezoelectric biocrystal thin films, Nat. Commun. 14 (2023) 6562, https://doi.org/10.1038/s41467-023-42184-8.
[38] W. Wang, P. Stipp, K. Ouaras, S. Fathi, Y. Huang, Broad bandwidth, self-powered acoustic sensor created by dynamic near-field electrospinning of suspended, transparent piezoelectric nanofiber mesh, Small 16 (2020) e2000581, https://doi.org/10.1002/smll.202000581.
[39] C. Lang, J. Fang, H. Shao, X. Ding, T. Lin, High-sensitivity acoustic sensors from nanofibre webs, Nat. Commun. 7 (2016) 11108, https://doi.org/10.1038/ncomms11108.
[40] Y. Wang, W. Gao, S. Yang, Q. Chen, C. Ye, H. Wang, Q. Zhang, J. Ren, Z. Ning, X. Chen, Z. Shao, J. Li, Y. Liu, S. Ling, Humanoid intelligent display platform for audiovisual interaction and sound identification, Nano-Micro Lett. 15 (2023) 221, https://doi.org/10.1007/s40820-023-01199-y.
[41] B. Lan, X. Xiao, A. Carlo, W. Deng, T. Yang, L. Jin, G. Tian, Y. Ao, W. Yang, J. Chen, Topological nanofibers enhanced piezoelectric membranes for soft bioelectronics, Adv. Funct. Mater. 32 (2022) 2207393, https://doi.org/10.1002/adfm.202207393.
[42] Z. Shao, X. Zhang, Z. Song, J. Liu, X. Liu, C. Zhang, Simulation guided coaxial electrospinning of polyvinylidene fluoride hollow fibers with tailored piezoelectric performance, Small 18 (2023) e2303285, https://doi.org/10.1002/smll.202303285.
[43] Y. Su, W. Li, X. Cheng, Y. Zhou, S. Yang, X. Zhang, C. Chen, T. Yang, H. Pan, G. Xie, G. Chen, X. Zhao, X. Xiao, B. Li, H. Tai, Y. Jiang, L. Chen, F. Li, J. Chen, High-performance piezoelectric composites via β phase programming, Nat. Commun. 13 (2022) 4867, https://doi.org/10.1038/s41467-022-32518-3.
[44] B. Chai, K. Shi, Y. Wang, Y. Liu, F. Liu, P. Jiang, G. Sheng, S. Wang, P. Xu, X. Xu, X. Huang, Modulus-modulated all-organic core–shell nanofiber with remarkable piezoelectricity for energy harvesting and condition monitoring, Nano Lett. 23 (2023) 1810–1819, https://doi.org/10.1021/acs.nanolett.2c04674.
[45] N. Shepelin, P. Sherrell, E. Skountzos, E. Goudeli, J. Zhang, V. Lussini, B. Imtiaz, K. Usman, G. Dicinoski, J. Shapter, J. Razal, A. Ellis, Interfacial piezoelectric polarization locking in printable $Ti_3C_2T_x$ MXene-fluoropolymer composites, Nat. Commun. 12 (2021) 3171, https://doi.org/10.1038/s41467-021-23341-3.
[46] Y. Wang, C. Huang, Z. Cheng, Z. Liu, Y. Zhang, Y. Zheng, S. Chen, J. Wang, P. Gao, Y. Shen, C. Duan, Y. Deng, C. Nan, J. Li, Halide perovskite inducing anomalous nonvolatile polarization in poly(vinylidene fluoride)-based flexible nanocomposites, Nat. Commun. 15 (2024) 3943, https://doi.org/10.1038/s41467-024-48348-4.
[47] N. Chocat, G. Lestoquoy, Z. Wang, D. Rodgers, J. Joannopoulos, Y. Fink, Piezoelectric fibers for conformal acoustics, Adv. Mater. 24 (2012) 5327–5332, https://doi.org/10.1002/adma.201201355.
[48] G. Tian, W. Deng, T. Yang, J. Zhang, T. Xu, D. Xiong, B. Lan, S. Wang, Y. Sun, Y. Ao, L. Huang, Y. Liu, X. Li, L. Jin, W. Yang, Hierarchical piezoelectric composites for noninvasive continuous cardiovascular monitoring, Adv. Mater. 36 (2024) 2313612, https://doi.org/10.1002/adma.202313612.